Research Square

Preprints are preliminary reports that have not undergone peer review.
They should not be considered conclusive, used to inform clinical practice,
or referenced by the media as validated information.

Study of Halfmetallic and Optoelectronic Characteristics of Ti 2 MnSb Inverse Heusler Alloy for Next Generation Sensors: First Principles Calculation

Vivek Kumar Jain
vivek.jain129@gmail.com

Poornima University
RaJesh Kumar
Poornima College of Engineering
Shiva Soni
Poornima University
Rakesh Jain
Mohanlal Sukhadia University
Archana Jain
Swami Keshvanand Institute of Technology, Management & Gramothan

Research Article

Keywords: Inverse Heusler alloys, electronic band structure, Ferrimagnetism, Optical Conductivity, Dielectric function

Posted Date: November 12th, 2026

DOI: https://doi.org/10.21203/rs.3.rs-11448587/v1

License: This work is licensed under a Creative Commons Attribution 4.0 International License.
Read Full License

Additional Declarations: No competing interests reported.

Study of Halfmetallic and Optoelectronic Characteristics of Ti_2MnSb Inverse Heusler Alloy for Next Generation Sensors: First Principles Calculation

Vivek Kumar Jain[1, *], Rajesh Kumar[2], Shiva Soni[1], Rakesh Jain[3], Archana Jain[4]

[1] Department of Physics, Faculty of Science and Humanities, Poornima University, Jaipur, Rajasthan, 303905, India

[2] Department of Physics, Poornima College of Engineering, Jaipur, Rajasthan, 302022, India

[3] Department of Physics, Mohanlal Sukhadia University, Udaipur, Rajasthan, 313001, India

[4] Swami Keshvanand Institute of Technology, Management and Gramothan, Jaipur, Rajasthan, 302017, India

*Email: vivek.jain@poornima.edu.in; vivek.jain129@gmail.com

Abstract

Halfmetallic characteristics of inverse Heusler alloy with formula Ti_2MnSb were investigated using WIEN2k based on density functional theory (DFT). Structure stable in an inverse Heusler alloy – Ti_2MnSb, with face centered cubic structure. The value of total magnetic moment was $2\mu_B$ at optimized lattice constant a_o = 6.33Å via energy vs volume curve for ferromagnetic case. Ti_2MnSb shows a half metallic ferromagnetic (HMF) behavior with an electronic energy band gap of 0.77eV in the minority spin of electronic band structure as well as in electronic density of states (EDOS). The electronic band structure, spin polarization, band gap and magnetic moment have been studied with effect of pressure in terms of lattice parameter variation using DFT under generalized gradient approximation (GGA). The optical characteristics at equilibrium lattice constant are presented within photon interaction of infrared, visible and ultraviolet energy in between 0 to 13.6 eV. These properties indicate the potential of Ti_2MnSb for spintronic applications.

Keywords: Inverse Heusler alloys, electronic band structure, Ferrimagnetism, Optical Conductivity, Dielectric function.

1. Introduction

Nowadays, optoelectronics and electronics-based spin devices are important research areas for the development of next-generation memory, sensing, and data-storage technologies. Calculations of the electronic structure which established the HMF and Heusler alloy such as NiMnSb by Groot in 1983, prompted interest in these materials for application in

spintronics devices [1]. Ti, Mn based Heusler alloys have attracted considerable research interest because of their diverse functional properties, including half-metallicity and spin-gapless behavior, as well as their potential applications in spintronic and related technologies [2-6]. Skaftouros et al. reported that Ti-based compounds can crystallize in the Hg_2CuTi-type inverse Heusler structure, in which the two Ti atoms occupy distinct neighboring sites [7-8]. Along this Ti_2MnZ with Z = Ga, Al, In, zero magnetic moment along with almost spin gapless behavior was reported by Jia et al [9]. Yadav et al. have employed the effects of lattice parameter variation as well as of the effect of cobalt addition on magnetism, spin polarization and optical properties of $Fe_{2-x}Co_xMnAl$ Heusler alloy for spintronics and photovoltaic device applications. Their results indicate all the alloys to be HM and ferromagnetic character at various ranges of lattice constants [10]. Deviations from the ideal lattice parameter and lattice distortions also occur on synthesis of materials for practical technological use in spintronics. Lattice variation study is thus important because during the alloy film preparation lattice variation occurs which may destroy the nature of HMF. Yang et al. reported results for Ti_2MnAl compound studied under pressure-strain condition using theoretical methods [11]. Yadav et al. reported that ball milling as well as pressure dependent in terms of lattice variation can affect the nature of HMF of Fe_2MnSn Heusler alloy incorporation in the value of spin polarization, bandgap and magnetic moment for application in spintronics devices [12-13]. Birsan et al. predicted Ti_2CoSi to exhibit as HMF by first principles calculation [14] for Co based alloys as their magnetic moment becomes high. Mn based alloys show better magnetic characteristics such as magnetic anisotropy, high curie temperature, high magnetic moment, magneto-optical effects in $Fe_{2-x}Co_xMnAl$, Fe_2MnZ alloys by Jain et al. [15-16]. Recent study on Mn based Heusler alloys shows phase transition between structural behalf as well as magnetism part [17-22]. Similarly, Ti based alloys shows various structure phase such as inverse Heusler phase, tetragonal phase, cubic phase in quaternary Heusler, half Heusler and full Heusler alloys for prominent applications in thermoelectric devices, spintronics as well as optical devices [23-30]. Previous studies of Rakesh et al. showed HMF in Ti_2MnSb alloys [31]. Zhang et al. employed a pseudopotential-based CASTEP method to investigate the structural, electronic, and magnetic properties of Ti_2MnZ (Z = Si, Ge, Sn, Sb, and Bi) compounds [32]. Although the electronic and magnetic properties of Ti_2MnSb have been reported previously, the present work focuses on a systematic investigation of its half-metallic, magnetic, and optical characteristics, with particular emphasis on the stability of half-metallicity under lattice-parameter variation. In addition, the optical response is analyzed over a broad photon-energy

range through the calculated optical conductivity, absorption coefficient, dielectric function, refractive index, extinction coefficient, reflectivity, and energy-loss function. The combined analysis provides a broader description of the electronic and optoelectronic response of Ti_2MnSb and its sensitivity to lattice variation.

"In the present work, the electronic band structure, magnetic properties, and optical characteristics of the Ti_2MnSb inverse Heusler alloy are investigated using the WIEN2k method. We also report the variation in the magnetic property, HMF and electronic band gap due to a change in the lattice parameter for potential applications in spintronics devices. Ths study also includes **optical conductivity, absorption coefficient, dielectric-function components (ε_1 and ε_2), refractive index, extinction coefficient, reflectivity, and energy-loss function**. These quantities highlight different aspects of the interaction between electromagnetic radiation and the electronic structure of Ti_2MnSb. For example, the absorption coefficient emphasizes photon-energy-dependent absorption, ε_1 and ε_2 describe the dispersive and absorptive dielectric response, while reflectivity and the energy-loss function provide information about surface reflection and collective electronic excitations, respectively. The present work is positioned as a **systematic combined electronic, magnetic, lattice-variation, and optical investigation** rather than as the first theoretical study of this compound.

2. Computational details

WIEN2k code based on DFT using the self-consistent and FP- LAPW method was used to determine the optoelectronic and magnetic characteristics such as band structure, magnetic moment, optical conductivity and dielectric functions etc [33-34]. The exchange correlation correction was done using the GGA given by Perdew–Burke–Ernzerhof [35]. The core and the valence energy threshold was set to −6.0 Ry between the states, Fourier expansion (G_{max}) was 12 $(a.u.)^{-1}$. The parameter for basis size control expansion, multiplication of muffin tin radius (R_{MT}) and maximum magnitude of reciprocal lattice vectors (K_{max} in interstitial region) used to be 8 in the plane-wave cutoff. The charge convergence criteria was set to be 10^{-4} e and 10^{-5} Ry was set as the energy convergence criterion. 3000 k-points were set to be for the full Brillouin zone (BZ) to integrate the BZ.

3. Result and Discussions

3.1. Structural properties

Figure 1(a) shows a crystal lattice view and figure 1(b) shows primitive cell view of the Ti_2MnSb inverse Heusler alloy from XCRYSDENSE. The Ti[A] and Ti [B] are at nearby as first nearest neighbor with position at (0,0,0) and (0.25, 0.25, 0.25) respectively, position of Mn at (0.5, 0.5, 0.5) and position of Sb at (0.75, 0.75, 0.75) in space group of 216 F43m.

The internal energy, $E(V)$, is found by integration of the pressure using Birch-Murnaghan Equation of state **[36]**:

$$E(V) = E_0 + \frac{9V_0B_0}{16}\left\{\left[\left(\frac{V_0}{V}\right)^{2/3} - 1\right]^3 B_0' + \left[\left(\frac{V_0}{V}\right)^{2/3} - 1\right]^2 \left[6 - 4\left(\frac{V_0}{V}\right)^{2/3}\right]\right\}. \quad (1)$$

The third-order Birch- Murnaghan isothermal equation of state is given by

$$P(V) = \frac{3B_0}{2}\left[\left(\frac{V_0}{V}\right)^{7/3} - \left(\frac{V_0}{V}\right)^{5/3}\right]\left\{1 + \frac{3}{4}(B_0' - 4)\left[\left(\frac{V_0}{V}\right)^{2/3} - 1\right]\right\}. \quad (2)$$

P is the pressure, V_0 is the reference volume, V is the deformed volume, B_0 is the bulk modulus, and B_0' is the bulk modulus derivative with respect to pressure. Typically, fits to experimental data yield the bulk modulus and its derivative, which are specified as

$$B_0 = -V\left(\frac{\partial P}{\partial V}\right)_{P=0} \quad B_0' = \left(\frac{\partial B}{\partial P}\right)_{P=0} \quad (3)$$

Figure 2 shows the curves between volume vs converged energy for non-magnetic (NM), ferro-magnetic (FM) cases and antiferromagnetic (AFM) phase. These curves show that optimized lattice volume for Ti_2MnSb in the Hg_2CuTi-type inverse Heusler structure is apparent that the FM phase configuration has a minimum converged energy as compared to the NM and AFM phases. The value of conserved energy is -18699.88725 Ry in the NM phase, -18699.90241 Ry in FM phase and -18699.87160 Ry for AFM phase. The energy difference for NM and FM phase is reported as 0.01516 Ry, 0.01565 Ry between NM and AFM phase and the energy difference for AFM and FM phase is 0.03081 Ry as the convergence criteria is set to be 0.00001 Ry in SCF cycle.

The value of the equilibrium lattice parameter is 6.33 Å in FM phase and the reported value by 6.33 Å by Rakesh et al. [31] and Zhang et al. as 6.31 Å for Ti_2MnSb [32]. While the optimized lattice parameters are 6.311 Å in the AFM phase and 6.320 Å in NM phase.

The calculated value of the bulk moduli is 141.4 GPa in FM phase, 150.43 GPa in NM phase and 276.57 GPa in AFM Phase.

The value of the pressure derivative of bulk moduli is 5.2 GPa in FM phase, -5.87 GPA in AFM phase and 4.58 GPa in NM phase. Its negative value in AFM shows unusual behaviour: an approaching phase transition where the atomic lattice becomes unstable and also causes elastic softening as the material's resistance to compression decreases as pressure increases [37]. While its positive value in FM and NM phase show that materials become harder to compress when pressure increases and stable phase.

By use of the equation (4) given below, the energy of formation ($E_{formation}$) has been calculated from which the stability of alloys has been examined.

$$E_{formation} = E_{Ti_2MnSb} - 2\,E_{Ti} - E_{Mn} - E_{Sb} \qquad (4)$$

Here, E_{Ti_2MnSb} is the equilibrium total energy of Ti_2MnSb and E_{Ti} for Ti; E_{Mn} for Mn; E_{Sb} for Sb per atom of the pure bulk structures respectively for Ti, Mn, Sb. Here we take the conversed energy as E_{Ti}= -1707.63570 Ry, E_{Mn}= -2317.29187 Ry, E_{Sb}= -12967.14386 Ry in equation 4. Value of $E_{formation}$ is observed to be -2.45 eV for FM, -2.66 eV for FM and -2.24 eV for AFM phase. The minimum energy of formation is observed in FM phase as a stable ground state phase for further calculations of electronic and optical properties.

Table 1: Energy of formation of the system for Ti_2MnSb in NM, FM and AFM phase.

Phase	E (Ry)	E_{Ti} (Ry)	E_{Mn} (Ry)	E_{Sb} (Ry)	$E_{formation}$ (Ry)	$E_{formation}$ (eV)
NM	-18699.88725	-1707.63570	-2317.29187	-12967.14386	-0.18012	-2.45
FM	-18699.90241	-1707.63570	-2317.29187	-12967.14386	-0.19528	-2.66
AFM	-18699.87160	-1707.63570	-2317.29187	-12967.14386	-0.16447	-2.24

The energy vs volume curve confirms the ground-state FM phase over the NM and AFM structure, though mechanical and dynamical stability remain unproven by these calculations alone. Elastic constants must be evaluated against Born criteria to determine mechanical stability, whereas phonon spectrum calculations are needed to verify dynamical stability. Such investigations lie outside the purview of this paper and call for further theoretical as well as experimental exploration.

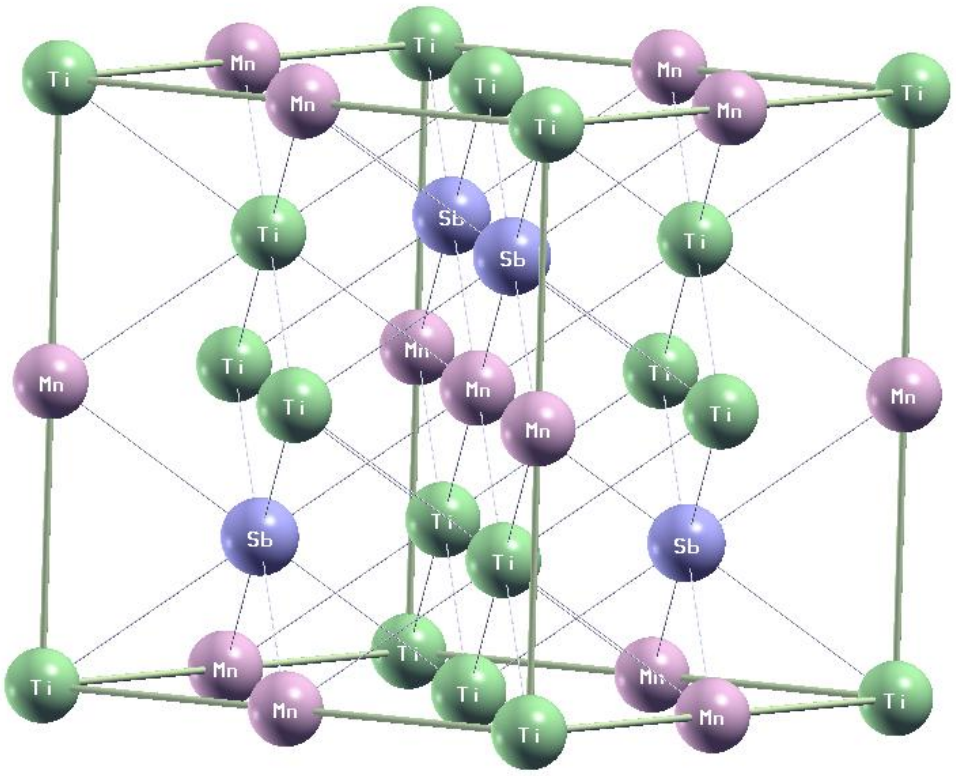


Figure 1(a) Crystal structure view of inverse Heusler alloy Ti_2MnSb

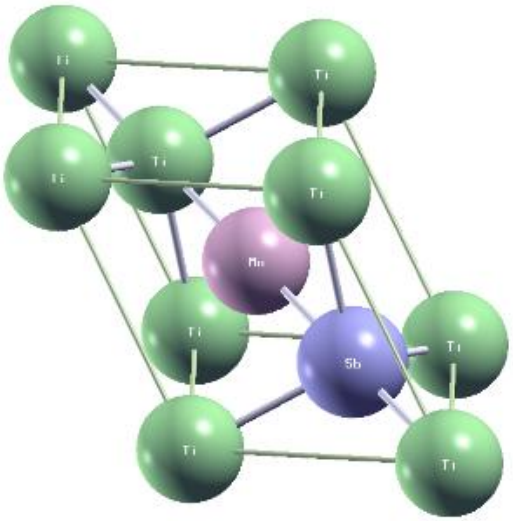


Figure 1(b) Primitive cell view of inverse Heusler alloy Ti_2MnSb

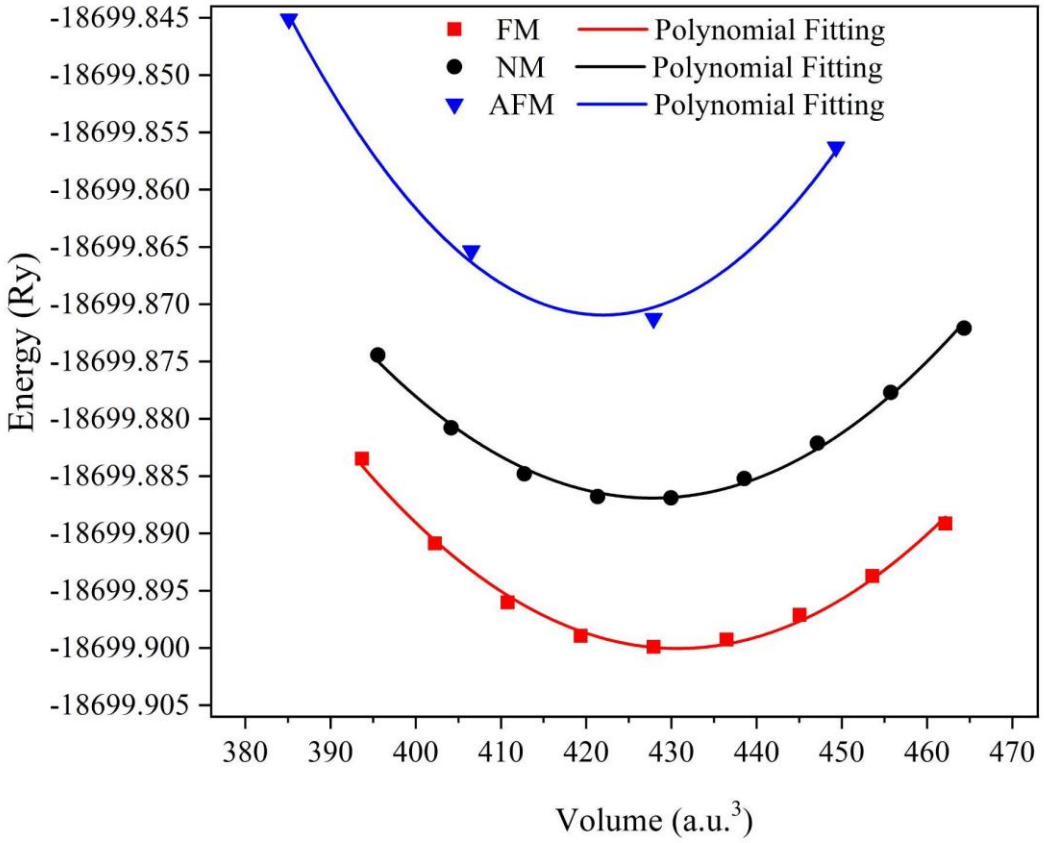


Figure 2 Volume and energy graph for non-magnetic (NM), farro-magnetic (FM) and antiferromagnetic structure in Ti_2MnSb

3.2. Electronic structure properties

The electronic density of states (EDOS) and electronic band structure for both minority and majority spin bands are shown in Figure 3. The predominant spin band is found to exhibit metallic characteristics in both the band and DOS and to be aligned with one another. Nonetheless, both band structure and DOS minority spin bands exhibit the semiconductor feature.

Values of the electronic energy gap for half metallic (E_{HM}) calculated using equation 5, and band gap (E_g) of the minority spin band calculated by equation 6 are shown in Table 2.

$$E_{HM}=E_F-E_{VBM} \quad (5)$$

$$E_g=E_{CBM}-E_{VBM} \quad (6)$$

The least energy needed to convert a minority-spin electron transition between the majority-spin Fermi level and VBM is known as the spin flip-gap for HMF (E_{HM}), and this energy level exhibits a spin-flipping gap. The band diagrams of the Ti_2MnSb Heusler alloy show the presence of an indirect energy band gap in the minority electronic spin bands, which has been calculated along the Γ point and L point. The value of indirect energy band gap is determined 0.77 eV in minority spin with the Fermi level located 0.52 eV above the VBM since the CBM is 0.25 eV above the Fermi level. The genuine HM character of Ti_2MnSb is indicated by the value of E_{HM} as 0.52 eV in the minority spin electronic band structure. Reported value of E_g 0.80 eV and E_{HM} 0.58 eV by Zhang et al. [32] at equilibrium lattice constant of 6.31 Å.

Total electronic densities of states (TEDOS) for Ti_2MnSb and partial electronic densities of states (PEDOS) computed for Ti at A and B sites with Mn and Sb atoms for the contribution of s, p, and d electrons are displayed in Figure 4. According to the TEDOS, majority spin shows metallic characteristics, whereas minority electronic spin presence semiconducting properties. While the *p* electronic states of Sb primarily dominates to the energy region in between -3.4 eV to -6.3 eV, the *s* electronic state of Sb adds to the range of energy from -10.2 to -11.4 eV below the level of Fermi Energy, which corresponds to the lowest energy zone. The 3*d* electronic states of Mn, Ti[B] and Ti[A] predominate in the area close to the Fermi level in both the valence and conduction bands (the numbers within the square brackets relate to the A and B sites in the Heusler structure). The contribution to the majority electronic spin band at the level of Fermi energy from 3*d* electronic states of the Ti[B] is less than that from 3*d* electronic states of the Mn and Ti[A].

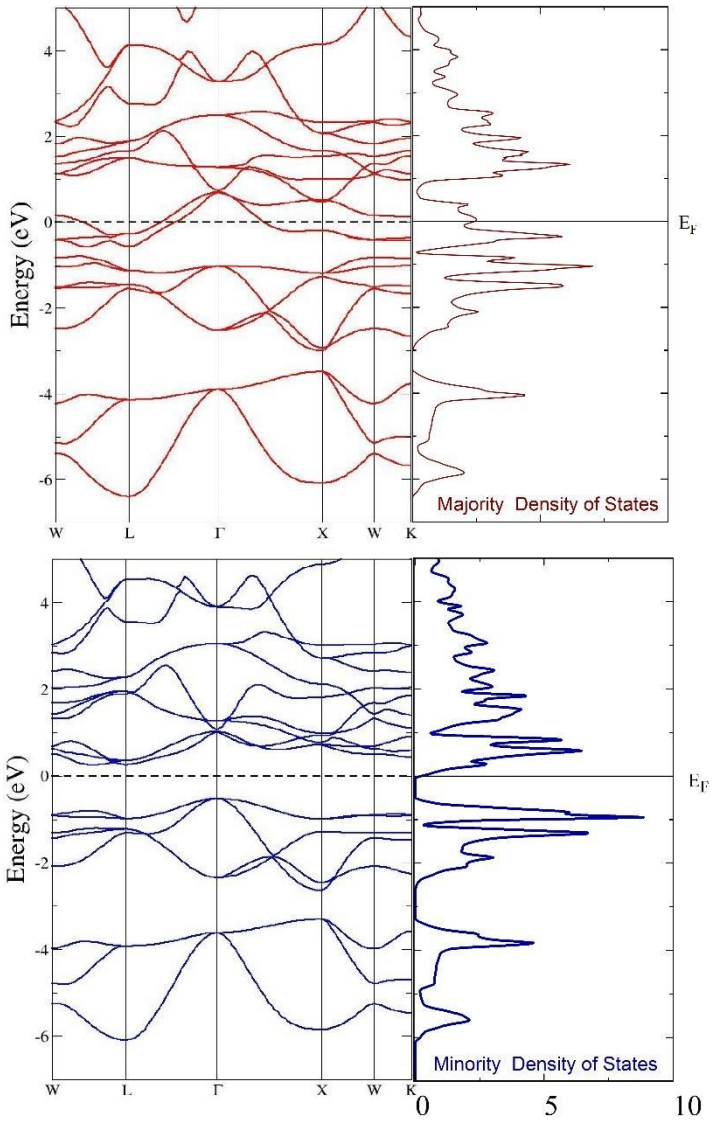


Figure 3 Electronic band structure diagrams of majority electronic spin density of states and minority electronic spin density of states for Ti_2MnSb

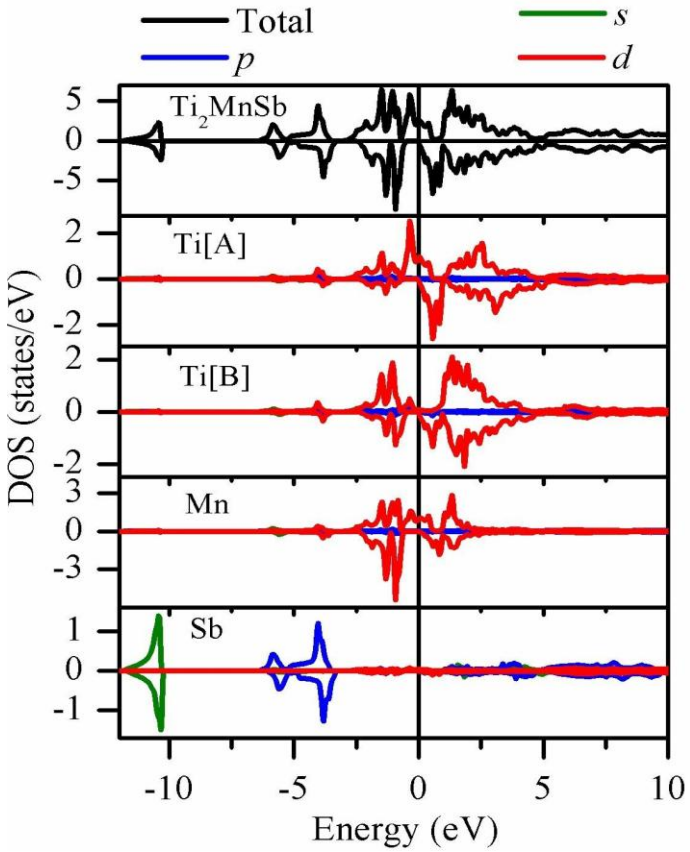


Figure 4 Total DOS of Ti_2MnSb and partial DOS of Ti [A/B site], Mn, Sb [taken from Ref. [31]]

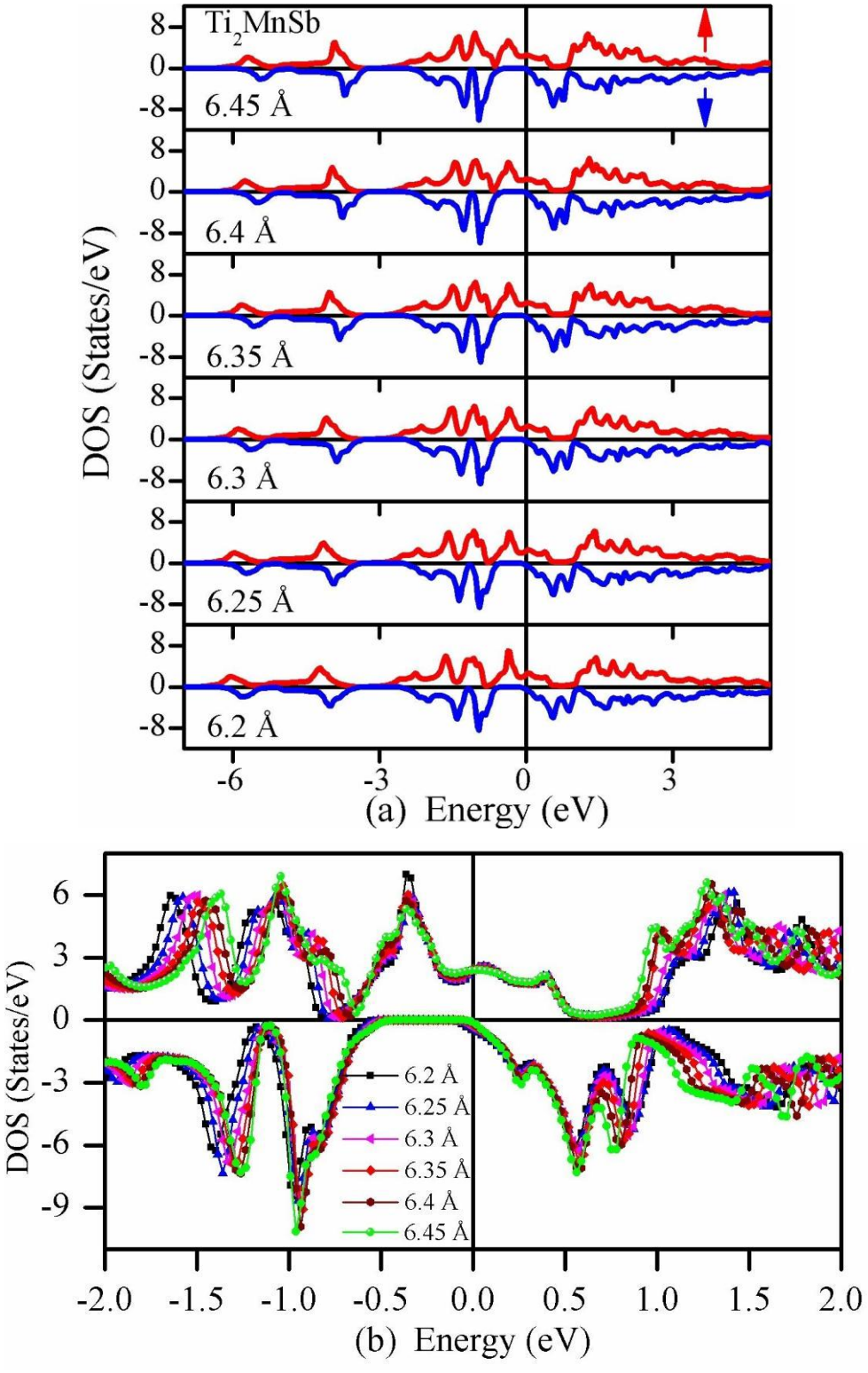


Figure 5 (a) DOS with variation of lattice parameter (b) Combined view of DOS with lattice parameter

The impact of lattice change on the TDOS is depicted in Figure 5 (a). Combine lattice variation TDOS, which is also depicted in Figure 5 (b), for more clarity. The growing peak height in the TDOS of Figure 5 (b) clearly illustrates how the number of electronic states per unit volume grows as the cell volume of the unit increases due to a rise in the lattice parameter. As the lattice parameter increases, TDOS peaks in the valence energy band and conduction energy bands move toward the levels of Fermi energy. The majority and minority spin band structures from 6.20 Å to 6.45 Å are displayed in Figure 6 in relation to DOS to explore the HMF nature as well as to calculate the value of E_g and E_{HM}. Majority spin band structure shows metallic behavior, while minority spin shows band gap and semiconductor behaviour for all the studied range of lattice parameters. Figure 7 shows the shift in the CBM and VBM with lattice variation is displayed to show the HM stability in minority spin. In the second part of this figure, change in band gap with lattice variation is shown. For a lattice variation from 6.20 Å to 6.45 Å of the lattice parameter of Ti_2MnSb, a variation in the minority spin electronic gap E_g is also observed from 0.85 eV to 0.69 eV as mention in Table 2.

Table 2: Electronic energy gap for half metallic (E_{HM}) and band gap (E_g) of the minority spin band with lattice variation

a (Å)	E_{HM} (eV)	E_g (eV)
6.20	-0.58	0.85
6.25	-0.56	0.82
6.30	-0.54	0.798
6.33	-0.52	0.77
6.35	-0.51	0.75
6.40	-0.5	0.73
6.45	-0.48	0.69

However, the sample loses its HMF nature for values of lattice parameters beyond 6.50 Å. Similarly, the value of E_{HM} varies from 0.62 eV to 0.46 eV in 6.20 Å to 6.45 Å respectively for flipping the spin as shown in figure 7. The electronic structure calculations were performed within the GGA-PBE approximation. Although semilocal DFT may underestimate absolute band-gap values and may not fully account for localized d-electron correlation, the present calculations are primarily used to investigate the half-metallic character and its stability against lattice-variation. At the equilibrium lattice parameter of 6.33 Å, a minority-spin indirect band gap of 0.77 eV is obtained, while the majority-spin

channel remains metallic. The minority spin electronic gap varies from 0.85 to 0.69 eV over the lattice-parameter range of 6.20–6.45 Å. Therefore, the present results establish the PBE-level electronic and magnetic trends of Ti_2MnSb. More advanced approaches, such as DFT+U, meta-GGA, or hybrid-functional calculations, would be useful in future work to assess the quantitative dependence of the band gap on exchange-correlation treatment.

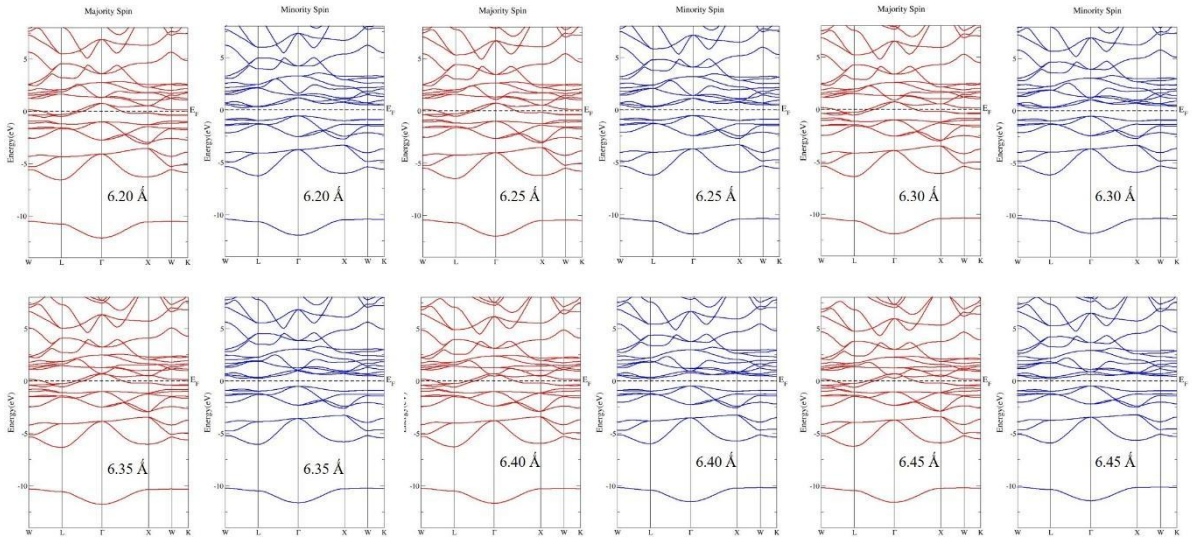


Figure 6: Band Structure Diagram with lattice-variation (red for majority electronic spin and blue for minority electronic spin)

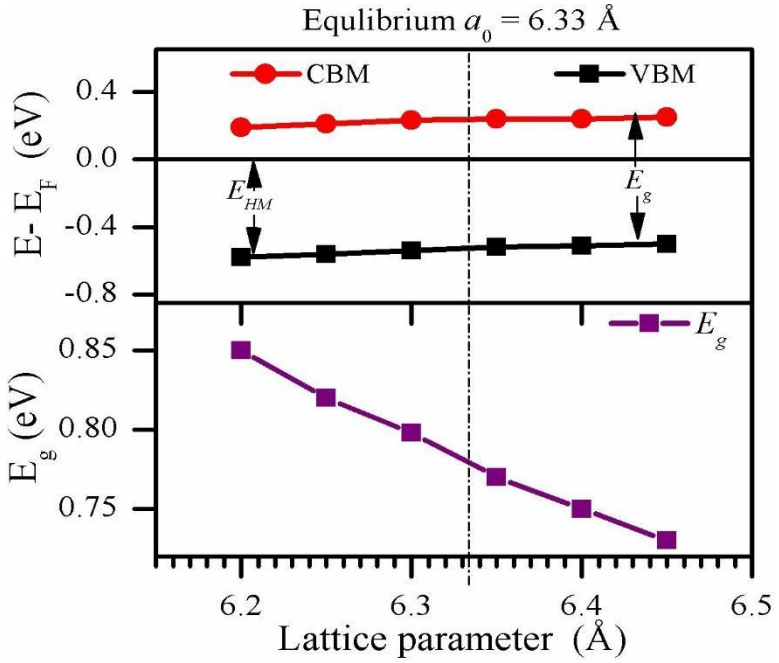


Figure 7 Electronic band gap variations with lattice parameter

3.3. Magnetic properties

The calculated total magnetic moment for the Ti_2MnSb using the Slater-Pauling rule given in equation (7):

$$M_{total} = N - 18 \quad (7)$$

According to the Slater–Pauling rule, the total magnetic moment of Ti_2MnSb can be estimated from the total number of valence electrons. Ti contributes 4 valence electrons, Mn contributes 7 valence electrons, and Sb contributes 5 valence electrons, giving a total of N = 2 × 4 + 7 + 5 = 20 valence electrons. Therefore, the expected total magnetic moment is 20 − 18 = 2 μ_B per formula unit. Atomic moments at individual values for Ti[A] and for Ti[B] are 1.235 μ_B, 0.512 μ_B respectively with parallel aligned to each other, while for Mn is -0.216 μ_B antiparallel aligned both Ti[A] and Ti[B] with Sb and negligible for Sb as 0.013 μ_B with interstitial moment 0.450 μ_B in total moment calculations. Because Ti[A] and Ti[B] have distinct nearest neighbors and next nearest neighbors, the value of magnetic moment of Ti[A] is seen to be nearly double that of Ti[B]. These results confirm the half-metallic and ferrimagnetic nature of Ti_2MnSb as previously reported with magnetic moment as 1.82 μ_B for Ti[A] ,0.88 μ_B for Ti[B] ,−0.6 μ_B for Mn[C] , −0.14 μ_B for Sb[D] [32].

Figure 8 illustrates how changes in lattice constant affect the total value of magnetic moment and moments of individual atoms for Ti_2MnSb. The total value of magnetic moment is essentially constant in the examined lattice range from 6.20 Å to 6.45 Å; it starts at 1.94 μ_B and thereafter approaches 2.00 μ_B. The moments of individual atoms of Ti[A] and Ti[B] grow as the lattice parameter increases. In the region under study, the value of magnetic moment of the atoms of Sb is nearly negligible, while the magnetic moment of the atom of the Mn as the lattice parameter increases. Its ferrimagnetic behavior is preserved in the examined lattice range because the negative sign of Mn moments also supports the opposite alignment to Ti[A] and Ti[B] moments.

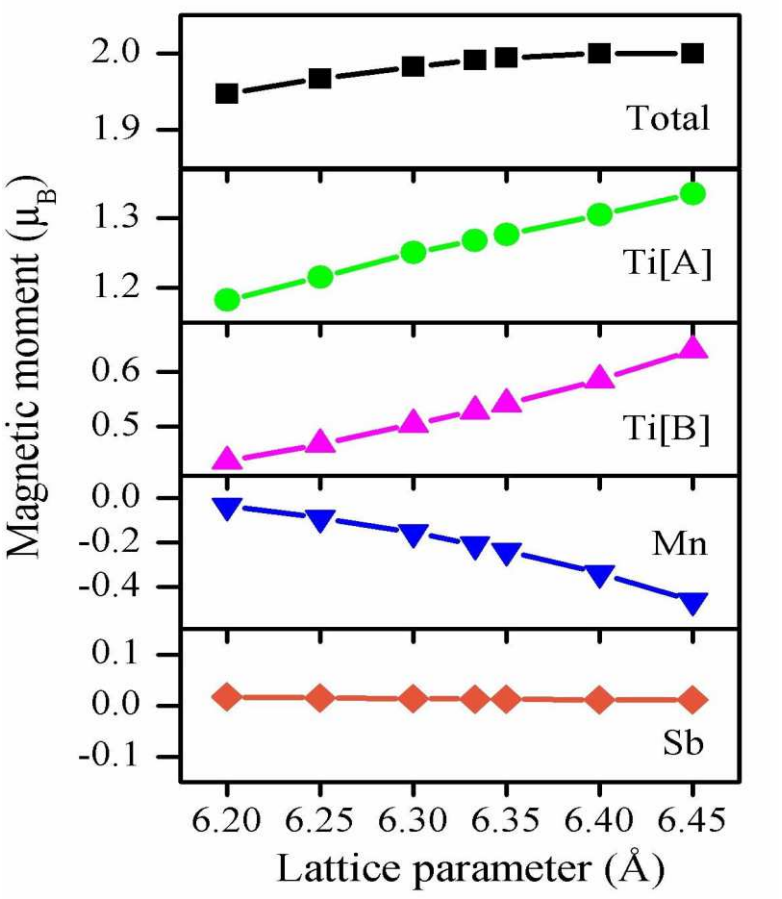


Figure 8 Total value of magnetic moments and values of magnetic moment of individual atoms in Ti_2MnSb with lattice variation.

3.4. Optical Properties

Behaviors of Optical characteristics of Ti_2MnSb with variation in energy of photon incident on alloys as shown in figure 9. Conductivity of Optics shown in Figure 9 (a) which is the material's ability to react to an electromagnetic energy—that is, photon-induced charge carrier excitation—is referred to as optical conductivity. Optical conductivity increases dramatically at low energies (IR region), suggesting free carrier (metallic-like) behavior. Interband electronic transitions are suggested by a prominent peak at ~1-2 eV. Beyond this, conductivity exhibits oscillations and progressively declines in the UV region, suggesting a lower chance of transformation at higher energy. This interpretation shows that Ti_2MnSb is the absorption spectrum is evidence of strong light–matter interaction in the visible–UV energy range. The frequency-dependent optical characteristics of Ti_2MnSb were computed via the PBE-GGA formalism, employing the complex dielectric function. This function is expressed as equation 8 [38]:

$$\varepsilon(\omega) = \varepsilon_1(\omega) + i\varepsilon_2(\omega) \tag{8}$$

Where $\varepsilon_1(\omega)$ and $\varepsilon_2(\omega)$ demotes the real as well as imaginary components of the dielectric function, correspondingly [**39,40**], can be derived by the subsequent relation via equation 9:

$$\varepsilon_1(\omega) = 1 + \frac{2}{\pi}\int_0^{\infty} \quad 1 * \frac{\omega' \varepsilon_2(\omega')}{\omega'^2 - \omega^2} d\omega' \tag{9}$$

The imaginary component ε_1 (ω) depicts the material's competence for absorbing along with losing energy, whereas the real part of dielectric function ε_1 (ω) generates its photonic reflection.

The absorption coefficient, α(ω), that measures the effectiveness of solar energy conversion is written as equation 10 **[40]:**

$$\boldsymbol{I(\omega) = \frac{2k\omega}{c}} \tag{10}$$

Coefficient of Absorption of Ti2MnSb is shown in figure 9(b) which represents the material's strength of light absorption is measured by its absorption coefficient. The absorption coefficient of Ti_2MnSb is low in the infrared region and increases substantially in the visible and ultraviolet regions, indicating strong interaction with incident electromagnetic radiation. These results characterize the optical response of Ti_2MnSb over the investigated photon-energy range. However, the calculated optical absorption alone does not establish photovoltaic absorber functionality or solar-cell performance. Therefore, the present study restricts the interpretation to the optical response of the half-metallic Ti_2MnSb alloy.

Dielectric Function's Real Part (ε_1) in figure 9(c) depicts the polarization response and dispersion. Strong polarization is indicated by high positive values at low energy. It crosses zero and turns negative about 2-3 eV. Plasma frequency is correlated with the zero-crossing point. In that area, metal-like reflectivity behavior is shown by a negative ε_1. However, Dielectric Function's Imaginary Part (ε_2) in figure 9(d) represents the absorption of energy as a result of electronic changes. It displays a prominent peak about 1-2 eV, which is indicative of interband transitions. Its value gradually drops with higher energies. This interpretation as the strong optical absorption caused by electron excitation is confirmed by high ε_2 in the visible region.

The polarizability of the material can be expressed by the equation below, and it is the most important factor which determines the refractive index, n(ω).

$$n(\omega) = \left(\frac{\varepsilon_1 + \sqrt{(\varepsilon_1^2 + \varepsilon_2^2)}}{2} \right)^{\frac{1}{2}} \tag{11}$$

The value of *n* of a material is frequency dependent and can be used as suitability of the materials for use in optical devices such as dispersion. This is an optical parameter which relates the proportion of the incident light reflected at an interface to the conditions under which total internal reflection occurs, such as the critical angle. The amount that light bends inside a substance is indicated by its refractive index (n) in figure 9 (g). it shows high value (~7–8) for low energy, which gradually drops as energy increases. It becomes comparatively low in the ultraviolet spectrum. It shows that strong light-matter interaction is suggested by a high refractive index in the visible spectrum. It is beneficial for waveguides and optical coatings.

Here k is the extinction parameter, which is represented by the following relation as equation 12 **[40],**

$$k(\omega) = \left(\frac{\sqrt{(\varepsilon_1^2+\varepsilon_2^2)}-\varepsilon_1}{2} \right)^{\frac{1}{2}} \tag{12}$$

Coefficient of Extinction (k) in figure 9 (h) symbolizes the material's internal light attenuation. It peaks at about 2 eV before progressively declining which has a similar tendency to ε_2. This correlates and verifies significant absorption corresponds to energy of the visible spectrum that decreases in the energy of the ultraviolet region.

The normal-incidence reflectivity is related to n and k through equation 13 as:

$$\boldsymbol{R(\omega)} = \frac{\boldsymbol{(n-1)^2+k^2}}{\boldsymbol{(n+1)^2+k^2}} \tag{13}$$

Reflectivity (R) is the amount of light reflected from a surface as indicated by reflectivity in figure 9 (f). Its value begins at a moderate level (~0.55), declines in the visible area, and then exhibits oscillations. It increases once more at higher energies (~0.7 in UV). Partial transparency/absorption balance due to moderate reflection in the visible range. Increased UV reflectivity leads to increased protection against high-energy radiation of this alloy.

The function for energy loss describes the transferred energy by a primary electron as it traverses material. This function can be expressed in terms of the complex dielectric function using the following relation by equation 14 **[38]**:

$$E_{loss}(\omega) = -Im(\varepsilon^{-1}) = \frac{\varepsilon_2}{\varepsilon_1^2+\varepsilon_2^2} \tag{14}$$

The maxima in the energy loss function, commonly referred to as plasmon resonances, occur when the value of ε_1 approaches zero while the value of ε_2 remains below unity (Figure

7).Function of Energy Loss (L) in figure 9 (e) represents the energy lost when rapid electrons move through a substance. It shows a prominent peak around ~12 eV. The plasma resonance, or plasma frequency, is represented by this peak and shows aggregate electron oscillations, or plasmons. The calculated optical functions are mutually related through the complex dielectric function and therefore exhibit correlated spectral features. For completeness, the principal optical quantities are presented and discussed in terms of their distinct physical significance. Rather than treating these quantities as independent evidence, their common spectral features are used to provide a consistent description of the electromagnetic response of Ti_2MnSb. Particular attention is given to the absorption behavior, dielectric response, reflectivity, and energy-loss function, which provide complementary information regarding photon–electron interactions and collective electronic excitations. The present study is based entirely on first-principles calculations and does not include experimental synthesis or characterization of Ti_2MnSb. Therefore, the calculated structural, electronic, magnetic, and optical properties should be regarded as theoretical predictions. Experimental studies are required to verify the formation and stability of the predicted inverse Heusler phase and to validate the calculated physical properties.

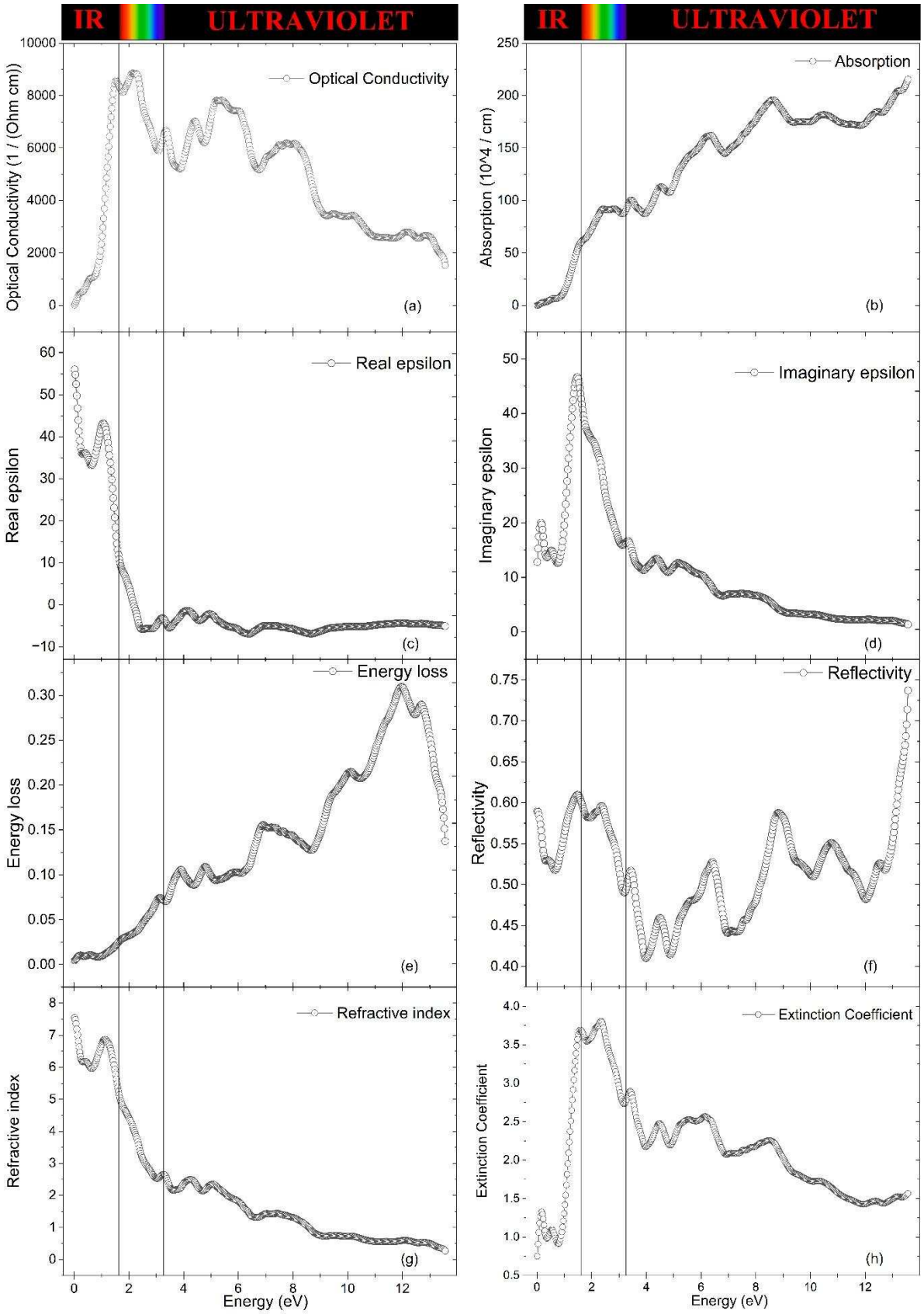


Figure 9 Optical Properties with variation of incidence photon energy

4 Conclusion

The optoelectronic and magnetic characteristics of Ti2MnSb, an inverse type of Heusler alloy with the Hg2CuTi type, were computed and studied using DFT implemented using the WIEN2k algorithm. Ti2MnSb was determined to be a HM and ferrimagnetic with an electronic energy gap of 0.77 eV in the minority-spin at 6.33 Å, the equilibrium value of the lattice constant and total value of magnetic moment of 2 μ_B. In the examined lattice range of 6.2 to 6.45 Å, the total magnetic moment is nearly constant. While the band gap ranges from 0.69 eV to 0.85 eV in this range of lattice constant, HMF nature of Ti_2MnSb is shown to be consistent over a range of investigated lattice parameters from 6.2 to 6.45 Å. Ti2MnSb is appropriate for spintronics because of all these characteristics. The electronic structure was calculated using the GGA-PBE exchange-correlation functional. The calculated minority-spin indirect band gap of 0.77 eV at the equilibrium lattice parameter of 6.33 Å should therefore be regarded as a GGA-PBE-level theoretical value. The quantitative band-gap value and the positions of the transition-metal d states may depend on the choice of exchange-correlation treatment. More advanced approaches, such as GGA+U or the modified Becke–Johnson (mBJ) potential, could be employed in future work to further examine the quantitative electronic structure of Ti_2MnSb.

Ti_2MnSb shows strong absorption in the visible–UV region and metal-like behavior in the infrared. It exhibits plasma resonance in the high-energy region and a high refractive index at low energies. The present calculations establish the optical properties of Ti_2MnSb—such as optical conductivity, absorption coefficient, dielectric response, refractive index, extinction coefficient, reflectivity, and energy-loss function. A limitation of the present first-principles investigation is that comprehensive thermodynamic, mechanical, and dynamical stability analyses have not been performed. In particular, formation energies relative to competing phases and convex-hull analysis are required to establish thermodynamic stability, while elastic constants and Born stability criteria are necessary for a complete assessment of mechanical stability. Phonon dispersion calculations would further be required to examine dynamical stability. Therefore, the present results establish the calculated electronic, magnetic, and optical characteristics of the proposed Ti_2MnSb inverse Heusler structure but do not by themselves demonstrate its thermodynamic or dynamical stability. Experimental synthesis and further theoretical stability investigations are necessary to assess its feasibility for practical spintronic and optoelectronic applications.

Acknowledgments

Rakesh Jain expressed his gratitude for the assistance he received in the form of the WIEN2k Code from the UGC-DSA and DST-FIST programs of the Physics Department at M L Sukhadia University in Udaipur. Shiva Soni and Vivek Kumar Jain expressed their gratitude to the Centre for Research, Instrumentation & Development (CRID) at Poornima University in Jaipur for their assistance. The Poornima University administration's seed money grant greatly aided in the effective completion of this research project.

Availability of data and materials

The correct structure parameters entered into the Density Function Theory within the WIEN2k Code, as specified in the computational details section, can reform the alloys described in this work. On reasonable request, the corresponding author can additionally provide data on these findings.

Conflict of Interests

The authors declare that there are no personal conflicts of interest associated with this research or its publication

Funding information

We announced that Poornima University has provided us with financial aid in the form of seed money grant no: PU/REG/2025-26/5283/3.

Contributions from the Author's

After reviewing the article, Vivek Kumar Jain wrote the main portion on alloy modelling and processing the findings. Shiva Soni and Rakesh Jain evaluate the research article, analyze the theoretical data, Archana Jain and Rajesh Kumar uses the data to construct Figures 1–9, and explain the results. All authors reviewed the manuscript.

Ethics declarations

Clinical trial registration: Not applicable
Consent to Publish declaration: Not applicable
Ethics and Consent to Participate declarations: Not applicable

References

1. RA De Groot, FM Muller, PG van Engen, KHJ Buschow, Phys Rev Lett 50:2024–2027 (1983).
2. Verma, S., Jain, V. K., Singh, J. P., Verma, A. S., Toual, Y., & Kamlesh, P. K. (2026). First-Principles Investigation of the Structural, Magnetic, Electronic, and Optical Properties of FeMnScB Quaternary Heusler Alloy. *International Journal of Nanoscience*.
3. Qin, X., & Yang, X. (2023). Theoretical design of Ti2-based magnetic shape memory alloys from first-principles. *Journal of Magnetism and Magnetic Materials*, *579*, 170876.
4. Jain, V. K., Lakshmi, N., Jain, R., & Jain, A. (2021). Structural, elastic, electronic, magnetic and optical properties of spin gapless semiconducting Heusler alloy Ti_2FeSb using first-principles calculations. *Journal of Electronic Materials*, *50*(10), 5857-5867.
5. Yu, M. (2023). *First Principles Simulation of Inorganic Materials and Interfaces by Density Functional Theory* (Doctoral dissertation, Carnegie Mellon University).
6. Zou, T., Jia, T., Xie, W., Zhang, Y., Widenmeyer, M., Xiao, X., & Weidenkaff, A. (2017). Band structure modification of the thermoelectric Heusler-phase TiFe 2 Sn via Mn substitution. *Physical Chemistry Chemical Physics*, *19*(28), 18273-18278.
7. Skaftouros, S., Özdoğan, K., Şaşıoğlu, E., & Galanakis, I. (2013). Generalized Slater-Pauling rule for the inverse Heusler compounds. *Physical Review B—Condensed Matter and Materials Physics*, *87*(2), 024420.
8. Skaftouros, S., Özdoğan, K., Şaşıoğlu, E., & Galanakis, I. (2013). Search for spin gapless semiconductors: The case of inverse Heusler compounds. *Applied physics letters*, *102*(2).
9. Yadav, A., & Jain, V. K. (2026). Effect of Cobalt Addition on Magnetism, Spin Polarization and Optical Properties of Fe2-xCoxMnAl Heusler Alloy for Spintronics and Photovoltaic Device Applications. *Journal of Superconductivity and Novel Magnetism*, *39*(3), 91.
10. Jia, H. Y., Dai, X. F., Wang, L. Y., Liu, R., Wang, X. T., Li, P. P., ... & Liu, G. D. (2014). Ti2MnZ (Z= Al, Ga, In) compounds: nearly spin gapless semiconductors. *AIP Advances*, *4*(4).
11. Wang, X., Cheng, Z., Yuan, H., & Khenata, R. (2017). L2 1 and XA ordering competition in titanium-based full-Heusler alloys. *Journal of Materials Chemistry*

C, *5*(44), 11559-11564.

12. Yadav, A., Jain, V.K. Study of Structural, Magnetic, Electronic, and Optical Properties of Fe_2MnSn Heusler Alloy. *J. Electron. Mater.* **54**, 7492–7502 (2025).
13. Yadav, A., Jain, V. K., Attatappa, V., Lakshmi, N., Sharma, A., Pandey, S. K., & Awasthi, S. (2025). Effect of temperature and Co-addition on phase stability, magnetic and electronic properties of Fe2-xCoxMnAl quaternary Heusler alloys for spintronics devices. *Journal of Alloys and Compounds*, *1027*, 180579.
14. Birsan, A., Palade, P., & Kuncser, V. (2013). Prediction of half metallic properties in Ti2CoSi Heusler alloy based on density functional theory. *Journal of magnetism and magnetic materials*, *331*, 109-112.
15. Jain, V. K., Lakshmi, N., Jain, R., & Chandra, A. R. (2019). Electronic Structure, Elastic, Magnetic, and Optical Properties of Fe2Mn Z (Z= Si, Ge, and Sn) Full Heusler Alloys: First-Principle Calculations. *Journal of Superconductivity and Novel Magnetism*, *32*(3), 739-749.
16. Jain, V. K., Lakshmi, N., Jain, R., Jain, V., Chandra, A. R., & Venugopalan, K. (2017). Electronic structure, magnetic and optical properties of quaternary Fe2− x Co x MnAl Heusler alloys. *Journal of materials science*, *52*(11), 6800-6811.
17. Idrissi, S., Ziti, S., Labrim, H., & Bahmad, L. (2021). Half-metallicity and magnetism in the full Heusler alloy Fe_2MnSn with L21 and XA stability ordering phases. *Journal of Low Temperature Physics*, *202*(3), 343-359.
18. Fan, L., Chen, F., Li, C. M., Hou, X., Zhu, X., Luo, J. L., & Chen, Z. Q. (2020). Promising spintronics: Mn-based Heusler alloys Mn3Ga, Mn2YGa (Y= V, Nb, Ta), ScMnVGa. *Journal of Magnetism and Magnetic Materials*, *497*, 166060.
19. Rameš, M., & Heczko, O. (2026). Universal Empirical Criterion for Martensitic Transformation Temperature in Ni-Mn-Based Heusler Alloys. *Metals*, *16*(1), 64.
20. Alexa, P., Životský, O., Uhlář, R., Kuča, D., Čegan, T., & Szurman, I. (2025). Fast neutron determination of bulk composition of Mn-based Heusler alloys. *Scientific Reports*, *15*(1), 9658.
21. Al-Douri, Y., & Ameri, M. (2025). Physical studies of spintronics-based Heusler alloys. *Critical Reviews in Solid State and Materials Sciences*, *50*(2), 189-238.
22. Asadian, A. R., Hakimi, M., & Ostovari, F. (2025). The remarkable effect of milling on the behavior of the Mn-based Heusler alloys: a comparative study on different

synthesis processes. *Physica Scripta*, *100*(12), 125924.

23. Bentouaf, A., Benaddi, F., Berrahal, M., Rached, A. A., & Belhadj, M. E. A. (2025). The half-metallic behavior of novel Ti2-based ternary Heusler compounds: ab initio study. *The European Physical Journal B*, *98*(11), 236.
24. Sharma, P. (2025). Lattice dynamics and thermal properties of TixZr1-xNiSn half-heusler alloys. *Alloys*, *4*(1), 3.
25. Parray, R. A., Mansoor, R., & Ravichandran, K. (2026). Influence of Annealing on Structural, Electrical, and Magnetic Properties of Ti2MnSn Inverse Heusler Alloy. *physica status solidi (a)*, *223*(5), e202500555.
26. Zhang, Y., Chen, D., Zhao, Y., Xiong, C., & Huang, Q. (2025). Experimental measurements of Ti–Sb binary phase diagram for half-Heusler thermoelectric alloys. *Bulletin of Materials Science*, *48*(2), 75.
27. Benichou, B., Bouchenafa, H., Bouabdallah, B., & Nabi, Z. (2025). Theoretical investigation of structural, elastic, mechanical, thermodynamic, electronic, and half-metallic ferromagnetic behavior of quaternary Ti2Fe-based full-Heusler alloys Ti2FeGe1-xSnx (x= 0, 0.25, 0.5, 0.75, and 1) for spintronic applications: DFT computation: B Benichou et al. *Indian Journal of Physics*, *99*(7), 2525-2541.
28. Mishra, S. R., Sankara Rama Krishnan, P. S., Davidson, K. P., Ramanujan, R. V., & Murty, B. S. (2025). Entropy Engineering in the Off-Stoichiometric Ti2NiCoSn0. 5Sb1. 5 Double Half-Heusler Alloy. *ACS Applied Energy Materials*, *8*(6), 3715-3731.
29. Khalil, A., Qasim, M., Ilyas, H., Andleeb, F., Yaqoob, U., Rafiq, M. A., & Rasul, M. N. (2025). Investigation of structural, electronic, phonon, optical and mechanical properties of CoBiX (X= Ti, Zr) direct bandgap semiconductors. *Materials Science in Semiconductor Processing*, *188*, 109238.
30. Yattung, T., Swain, P. K., & Mohanta, S. K. (2025). Ab initio investigation of structural, electrical, optical, and thermoelectric properties of the half-heusler alloy MnTiAs. *Materials Chemistry and Physics: Sustainability and Energy*, *2*, 100006.
31. Jain, R., Jain, V. K., Lakshmi, N., Chandra, A. R., Venugopalan, K., & Jain, V. (2017). First principle calculation of half metallicity in Ti_2MnSb Heusler alloy. *AIP Conference Proceedings*, *1832*(1), 090007.
32. Zhang, L., Wang, L. Y., Lu, J. J., Wang, X. T., & Wang, L. (2014). Ti_2Mn Z (Z= Si, Ge, Sn, Sb, Bi) compounds: A first-principles study of electronic structures and magnetism. *Journal of the Korean Physical Society*, *65*(12), 2058-2065.

33. Schwarz, K., Blaha, P., Madsen, G. K., Kvasnicka, D., & Luitz, J. (2001). An augmented plane wave+ local orbitals program for calculating crystal properties. *Institut Für Physikalische und Theoretische Chemie: Vienna, Austria*.
34. Blaha, P., Schwarz, K., Tran, F., Laskowski, R., Madsen, G. K., & Marks, L. D. (2020). WIEN2k: An APW+ lo program for calculating the properties of solids. *The Journal of chemical physics*, *152*, 074101.
35. Perdew, J. P., Burke, K., & Ernzerhof, M. (1996). Generalized gradient approximation made simple. *Physical review letters*, *77*, 3865.
36. Birch, F. (1986). Equation of state and thermodynamic parameters of NaCl to 300 kbar in the high-temperature domain. *Journal of Geophysical Research: Solid Earth*, *91*(B5), 4949-4954.
37. Pandit, A., & Bongiorno, A. (2023). First-principles calculation of the pressure derivative of the bulk modulus from second-and third-order elastic constants. Physical Review Materials, 7(7), 073801.
38. Toll, J. S. (1956). Causality and the dispersion relation: Logical foundations. *Physical Review, 104*(6), 1760-1770.
39. Ambrosch-Draxl, C., & Sofo, J. O. (2006). Linear optical properties of solids within the full-potential linearized augmented plane-wave method. *Computer Physics Communications, 175*(1), 1-13.
40. Belmiloud, N., Boutaiba, F., Belabbes, A., Ferhat, M., & Bechstedt, F. (2016). Half-Heusler compounds with a 1 eV (1.7 eV) direct band gap, lattice-matched to GaAs (Si), for solar cell application: A first-principles study. *Physica Status Solidi B, 253*(5), 889-894.